Nano Research

Open Access

Research Article

Waste cotton fabric promotes high-entropy carbide ceramics nanowires growth to achieve high-performance electromagnetic interference shielding

Huimin Liu[1], Yingjun Sun[1], Xin Zhang[1], Bing Liu[1], Liyuan Han[3], Qiangang Fu[1], Xuemin Yin[1,2] ✉, and Hejun Li[1] ✉

[1] *State Key Laboratory of Solidification Processing, Shaanxi Key Laboratory of Fiber Reinforced Light Composite Materials, Carbon/Carbon Composites Research Center, Northwestern Polytechnical University, Xi'an 710072, China*
[2] *Department of Aeronautical and Aviation Engineering, The Hong Kong Polytechnic University, Hung Hom, Kowloon, Hong Kong 999077, China*
[3] *Henan Key Laboratory of High Performance Carbon Fiber Reinforced Composites, Institute of Carbon Matrix Composites, Henan Academy of Sciences, Zhengzhou 450046, China*

Cite this article: *Nano Research*, **2025**, *18*, 94907749. https://doi.org/10.26599/NR.2025.94907749

ABSTRACT: One-dimentional high-entropy metal carbides have attracted significant attention for their exceptional physical and chemical properties, which endow them with great potential for applications in structural and functional fields. However, there is a lack of stable preparation methods, particularly on flexible substrates. In this study, we successfully synthesized high-entropy $(Ti_{0.2}Zr_{0.2}H_{f0.2}Nb_{0.2}Ta_{0.2})C$ (HEC) nanowires through a precursor pyrolysis method using waste cotton fabric as both a flexible substrate and a carbon source. Interestingly, the growth of the nanowires followed a catalyst-assisted vapor–liquid–solid mechanism, driven by the dissolution of metals and carbon-containing molecules originating from the polymer precursors and thermal decomposition of cotton fabric in the Fe-Ni alloy. This process involved nucleation of HEC and subsequent nanowire growth. The as-prepared HEC nanowires with diameters ranging from 0.05 to 0.1 μm were randomly distributed on carbonized cotton fiber substrate without a specific orientation, forming an interconnected multiscale conductive network. Owing to the synergistic effects including electrical conduction loss, dipolar polarization loss arising from lattice distortion in HEC, and polarization loss generated by numerous heterojunctions within the material, the prepared HEC nanowires exhibit outstanding electromagnetic interference (EMI) shielding performance in the X-band (8.2–12.4 GHz). For instance, the material achieved an EMI shielding effectiveness (SE) of 57.55 dB at a thickness of 1.35 mm. This study introduces novel perspectives and scalable approaches for the preparation, formation mechanism, and functional applications of nanostructured high-entropy ceramics.

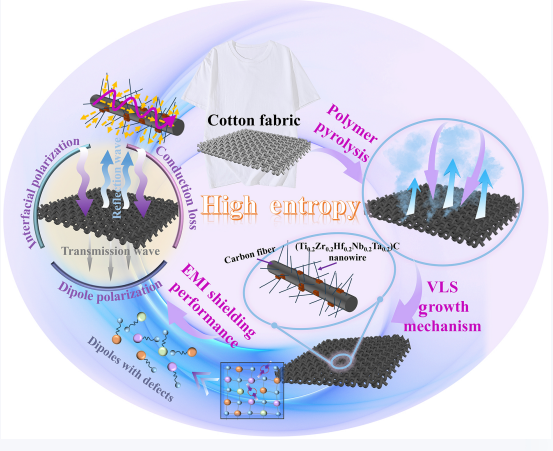

KEYWORDS: high-entropy, $(Ti_{0.2}Zr_{0.2}Hf_{0.2}Nb_{0.2}Ta_{0.2})C$ nanowires, growth mechanism, electromagnetic interference shielding performance

1 Introduction

One-dimensional (1D) ceramic materials have emerged as a research hotspot in materials science due to their unique geometric structures and physicochemical properties [1]. The high aspect ratio of 1D structures endows these materials with outstanding mechanical properties, including high strength, high modulus, and superior fracture toughness [2]. Additionally, their nanoscale dimensions further enhance thermal and chemical stability. Through innovative material design and preparation techniques, our group has successfully developed a series of high-performance 1D ceramic materials and systematically explored their applications in nanoscale reinforcing phases, energy storage, and electromagnetic materials [3–6].

Received: May 13, 2025; **Revised:** June 19, 2025
Accepted: June 30, 2025

✉Address correspondence to Xuemin Yin, yinxuemin@nwpu.edu.cn; Hejun Li, lihejun@nwpu.edu.cn

In recent years, high-entropy ceramics have garnered significant attention as a novel ceramic material system owing to their distinctive high-entropy effects [7–11]. Unlike traditional ceramics, high-entropy ceramics exhibit superior oxidation resistance and thermal stability in high-temperature environments, along with remarkable improvements in mechanical properties, corrosion resistance, and electrical conductivity [12, 13]. These characteristics make them potential contenders for utilization in mechanical, thermal, electrical, and magnetic fields. Among various high-entropy ceramic systems, high-entropy carbide ceramics have become a key research focus because of their outstanding high-temperature performance and multifunctionality [8, 14–17]. Despite significant progress in the study of high-entropy carbide ceramics, research on 1D structures remains limited [18]. Combining the geometric advantages of 1D structures with the performance benefits of high-entropy effects, these materials hold potential for structural and functional materials. For example, Ma et al. synthesized $(Ta_{0.25}Hf_{0.25}Ti_{0.25}Nb_{0.25})C$ high-entropy metal carbide nanowires via a bamboo-based carbothermal method demonstrating exceptional thermal stability with no morphological changes below 1600 °C [14]. However, current research primarily focuses on powdered 1D high-entropy carbides, which face limitations in direct integration into structural or functional materials. The need for additional processing steps compromises structural controllability, mechanical stability, and functional integration, limiting the full utilization of their 1D structural advantages. For instance, *in situ* growth of 1D ceramic nanowires on carbonaceous substrates could enable binder-free supercapacitor electrodes, simplifying device fabrication. More importantly, previous research on 1D high-entropy carbide ceramics has centered on thermophysical and high-temperature properties, with limited exploration of functional applications and underlying mechanisms.

Integrating high-entropy metal carbide nanowires with a substrate not only enhances the mechanical characteristics and stability of the nanowires, but also expands the adaptability in practical applications. In this work, we successfully synthesized high-entropy metal carbide $(Ti_{0.2}Zr_{0.2}Hf_{0.2}Nb_{0.2}Ta_{0.2})C$ (HEC) on a flexible cotton fabric substrate via a polymer pyrolysis method (Fig. 1). The growth mechanism of HEC nanowires was the classical vapor–liquid–solid (VLS) process. Cotton fabric served as an *in situ* growth substrate for HEC nanowires, uniformly adsorbing the precursor solution during impregnation and also providing carbon sources for nanowire growth. Meanwhile, the HEC nanowires exhibited excellent electromagnetic interference (EMI) shielding performance, achieving an EMI shielding effectiveness (SE) of 37.07 dB at 0.45 mm thickness and 57.55 dB at 1.35 mm thickness. This work provides new insights and the methodology for the fabrication, formation mechanisms, and functional applications of high-entropy nanomaterials.

2 Experimental

2.1 Fabrication of HEC nanowires

The raw material for fabricating HEC nanowires was a commercially available liquid precursor purchased from the Chinese Academy of Sciences, consisting of $(Ti_{0.2}Zr_{0.2}Hf_{0.2}Nb_{0.2}Ta_{0.2})$ C-containing polymer precursor (15 wt.%–30 wt.%) dissolved in xylene.

The present work utilized flexible cotton fabric as the substrate. HEC nanowires were obtained by carbothermal reduction reaction with catalyst. The preparation process was schematically illustrated in Fig. 2. An appropriate amount of polymer precursor and catalysts ($Fe(NO_3)_2{\cdot}9H_2O$, $Ni(NO_3)_2{\cdot}6H_2O$, and NaF) were weighed in a beaker at a mass ratio of 1:0.05–0.2:0.05–0.2:0.15–0.3. An appropriate amount of xylene solution was incorporated. And the mixture was stirred by employing a magnetic stirrer under room

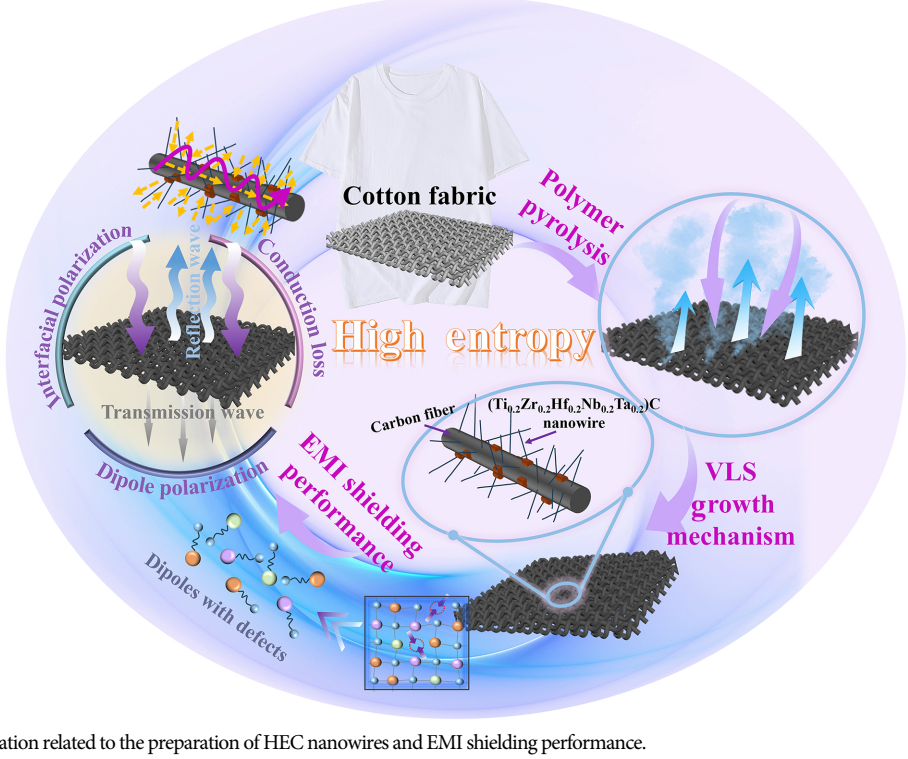

Figure 1 Schematic illustration related to the preparation of HEC nanowires and EMI shielding performance.

Figure 2 The schematic diagram of the preparation process.

temperature until the solution became homogeneous. The precursor and catalysts were fully dissolved and mixed uniformly in the xylene solution. The waste cotton fabric was immersed in the solution for 8 min and dried in an oven at 70 °C. The cotton fabric was placed in an alumina crucible and heated in a tube furnace to 900–1400 °C at 5 °C/min, then held for 2 h in Ar atmosphere. A black layer on the surface of the carbonized cotton fabric could be observed, which was identified as HEC nanowires. The samples prepared at 900, 1150, and 1400 °C were named HEC-900 °C, HEC-1150 °C, and HEC-1400 °C, separately.

2.2 Characterizations

Fourier transform infrared spectroscopy (FT-IR, IRTracer 100) was employed to analyze the molecular structure of the single-source polymer precursors. The polymer-to-ceramic transformation was studied via thermogravimetric and derivative thermogravimetric coupled with mass spectrometry (TG-DTG-MS, NETZSCH-NETZSCH-QMS 403 D + STA 449 F3 +ThermoFisher-Nicolet iS20) to assess the yield and composition of the precursors. The synthesized materials were characterized for their morphology and microstructure using transmission electron microscopy (TEM, Talos F200X) combined with energy-dispersive X-ray spectroscopy (EDS) and scanning electron microscopy (SEM, FEI NovaNano 450). Using X-ray diffraction (XRD, X'Pert PRO MPD), the phase composition of the HEC nanowires was evaluated. The bonding characteristics were analyzed using X-ray photoelectron spectroscopy (XPS) with a Thermo Fisher ESCALAB Xi+ instrument. The electrical conductivity was assessed through a two-probe measurement technique.

2.3 EMI shielding measurements

Employing an Anritsu MS4644A vector network analyzer, electromagnetic shielding characteristics were investigated in 8.2 to 12.4 GHz (X-band) through S-parameter analysis. The evaluation was performed on rectangular samples with dimensions of 22.86 by 10.16 mm. The scattering parameters (S_{11}, S_{12}, S_{21}, S_{22}) were applied to compute fundamental electromagnetic coefficients: $R = |S_{11}|^2 = |S_{22}|^2$ for reflection, $T = |S_{21}|^2 = |S_{12}|^2$ for transmission, and $A = 1 - R - T$ for absorption. The shielding effectiveness was analyzed by three components: reflection shielding ($SE_R = -10\log(1 - R)$), absorption shielding ($SE_A = -10\lg[T/(1 - R)]$)), and multiple reflections (SE_M). The total shielding effectiveness (SE_T) was obtained by summing these individual contributions ($SE_T = SE_R + SE_A + SE_M$). In cases where the absorption shielding effectiveness exceeded 15 dB, the multiple reflection effect could be considered negligible [19, 20].

3 Results and discussion

Herein, HEC nanowires were *in situ* grown on the substrate of waste cotton fabric through carbothermal reduction. To better understand the growth mechanism of HEC nanowires, the molecular structure of the $(Ti_{0.2}Zr_{0.2}Hf_{0.2}Nb_{0.2}Ta_{0.2})C$-containing polymer precursor was first investigated by FT-IR, as shown in Fig. 3(a). The stretching vibrations observed at 1024 and 835 cm^{-1} in M–O–C bonds (M = Nb, Zr, Hf, Ta, and Ti) could be attributed to the reactions between the transition metal chlorides, acetylmethane and butanol. Additional transmittance bands of C–O at 1374 and 1271 cm^{-1}, C=C at ~ 1529 cm^{-1}, C–C at 1433 cm^{-1}, C=O at 1593 cm^{-1}, and C–H at 2868 and 2922 cm^{-1} were due to either the acetylacetone ligand at the side chain or the terminal group of the preceramic polymer [21, 22]. The peak at ~ 3442 cm^{-1} was connected with the O–H stretching vibration in H_2O from moisture adsorbed on the specimen surfaces. The detection of M–O–M′ bond (M′ = Nb, Zr, Hf, Ta, and Ti) at ~ 657 cm^{-1} clearly demonstrated that the condensation of transition metal alkoxides had already occurred during the polymerization process.

The pyrolysis behavior for $(Ti_{0.2}Zr_{0.2}Hf_{0.2}Nb_{0.2}Ta_{0.2})C$-containing polymer precursor loaded on cotton fabric was investigated using TG-DTG-MS (Fig. 3(b)). Based on the slope changes of the curves, the pyrolysis of the precursor was divided into three stages with increasing temperature (Fig. 3(b)(1)). In the first stage, a weight loss of around 2.54% was observed below 200 °C, primarily caused by the dehydration of hydroxyl groups as well as the emission of H_2O,

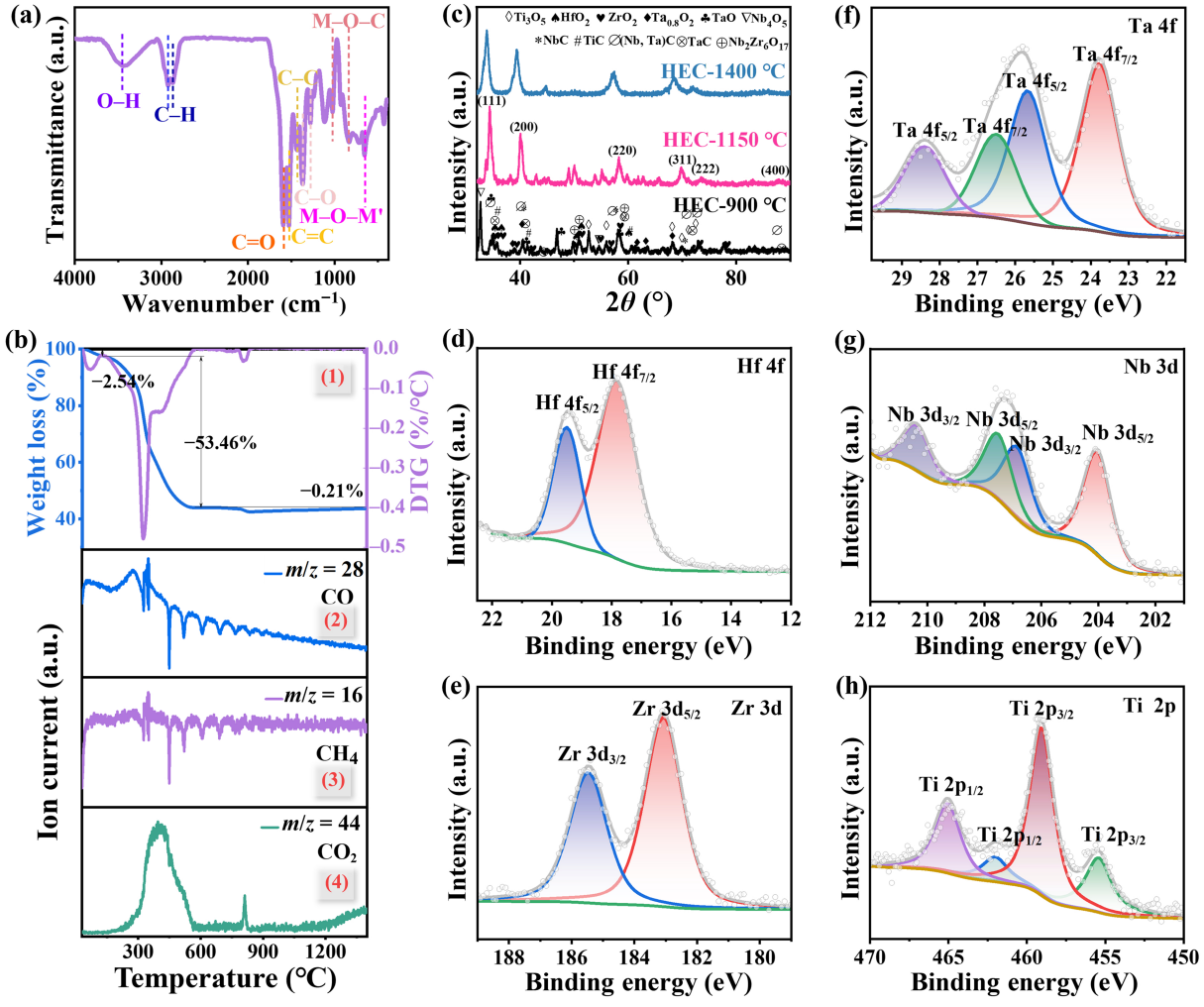

Figure 3 (a) FT-IR spectrum of $(Ti_{0.2}Zr_{0.2}Hf_{0.2}Nb_{0.2}Ta_{0.2})$C-containing polymer precursor powder. (b) (1) TG-DTG curves and MS spectra ((2) CO (m/z = 28), (3) CH_4 (m/z = 16), and (4) CO_2 (m/z = 44)) of $(Ti_{0.2}Zr_{0.2}Hf_{0.2}Nb_{0.2}Ta_{0.2})$C-containing polymer precursor on cotton fabric. (c) XRD patterns of samples prepared at different temperatures. XPS survey spectra of HEC-1150 °C: (d) Hf 4f, (e) Zr 3d, (f) Ta 4f, (g) Nd 3d, and (h) Ti 2p.

with a corresponding derivative DTG peak at about 100 °C. The second stage occurred between approximately 200 and 600 °C, involving the main organic–inorganic transformation, resulting in a weight loss of 53.46%. Rearrangement of ligands and cleavage of molecular carbon chains occurred, accompanied by the release of H_2O (m/z = 18, m/z = 17, Fig. S1 in the Electronic Supplementary Material (ESM)), CO (m/z = 28, Fig. 3(b)(2)), CH_4 (m/z = 16, Fig. 3(b)(3)), CO_2 (m/z = 44, Fig. 3(b)(4)). These small carbon-containing molecules from polymer precursor and cotton fabric provided carbon sources for the generation of HEC nanowires. The third stage might be the carbothermal reduction, which and a ceramization process, consuming CO (m/z = 28, Fig. 3(b)(2)), CH_4 (m/z = 16, Fig. 3(b)(3)) and resulting in the release of CO_2 (m/z = 44, Fig. 3(b)(4)), with a weight loss of 0.21% [23]. Overall, the polymer precursor undergoes cross-linking, organic–inorganic transformation, and a ceramization process [24].

The phase evolution observed by XRD was in good agreement with the TG-MS results (Fig. 3(c)). After heating to 900 °C, the carbides and oxides such as HfO_2, ZrO_2, (Nb, Ta)C, TiC could be detected because of incomplete carbothermal reduction. When the temperature increased to 1150 °C, distinct diffraction peaks assigned to (111), (200), and (220) could be observed. The HEC nanowires possessed a single carbide crystalline phase. As the temperature increased to 1400 °C, the crystallinity of HEC was obviously enhanced, while almost no residual oxides or carbides were detected.

The chemical bonding states of HEC nanowires were analyzed using XPS. Figures 3(d)–3(h) showed the high-resolution XPS patterns of HEC. Four peaks could be identified by deconvoluting the C 1s peak (Fig. S2 in the ESM). Among them, the peak at 282.8 eV corresponded to C–M bond (M = Zr, Hf, Ta, Ti, and Nb), indicating bonds between transition metals and carbon [25]. The other three peaks centered at 289.6, 286.4, and 284.8 eV corresponded to O–C=O, C–O, and C–C [26]. In the Hf 4f spectrum of Fig. 3(d), the peak at 17.8 eV was assigned to Hf $4f_{7/2}$ of the Hf–C bond, whereas the peak at 19.5 eV was attributed to Hf $4f_{5/2}$ of the Hf–O bond [12, 27]. The Zr $3d_{3/2}$ at 185.5 eV was related to Zr–O, while Zr $3d_{5/2}$ peak at 183.0 eV corresponded to Zr–C (Fig. 3(e)) [25, 28]. And a doublet at 23.8 and 25.7 eV indicated Ta–C in Ta 4f spectrum, along with a weak doublet at 26.5 and 28.4 eV connected with Ta–O (Fig. 3(f)) [29]. As displayed from Nb 3d in Fig. 3(g), peaks at 207.6 and 210.4 eV corresponded to the $3d_{5/2}$ and $3d_{3/2}$ states of the Nb–O bond. Peaks at 204.0 and 206.9 eV were assigned to the $3d_{5/2}$ and $3d_{3/2}$ states of the Nb–C

bond [30]. In the Ti 2p spectra (Fig. 3(h)), peaks at 462.0 and 455.4 eV were attributed to Ti $2p_{1/2}$ and $2p_{3/2}$ of the Ti–C bond, while the peaks at 459.0 and 465.0 eV corresponded to Ti–O bond [31]. Metal–O may originate from oxygen adsorbed on the surface of the material or oxides produced during the synthesis of the material. The existence of metal–O bonds may increase the heterogeneous interfaces within the material, generating interface polarization phenomena and dissipating the energy of electromagnetic waves. In summary, the XPS data confirmed the presence of chemical bonds between the carbon and metal elements within the HEC nanowires.

As shown in Figs. 4(a)–4(c), SEM images revealed the products obtained at different heat treatment temperatures. At 900 °C, no HEC nanowires were observed. Instead, the surface of the carbonized cotton fiber (CCF) was predominantly covered with micro-nano particles of different sizes (Fig. 4(a)). Combined with XRD analysis, these particles were identified as oxide and carbide ceramic particles corresponding to the early reaction stage. As the temperature increased to 1150 °C, many HEC nanowires were observed on the substrate surface, along with some ceramic particles (Fig. 4(b)). The nanowires were randomly distributed without a fixed orientation, with diameters ranging from 0.05 to 0.1 μm. At 1400 °C, fewer HEC nanowires were observed on the substrate surface, while ceramic particle density increased (Fig. 4(c)). This occurred because atomic mobility and diffusion capacity (particularly at grain boundaries) increase with temperature. Excessive grain growth at 1400 °C caused near-complete transformation into ceramic particles before nanowire formation [32].

As shown in Fig. 4(d), the XRD pattern of HEC nanowires synthesized at 1150 °C was Rietveld-refined based on a cubic crystal system with the Fm-3m space group. The results indicated that the synthesized HEC-1150 °C consisted of a single carbide phase. More importantly, HEC-1150 °C could withstand bending and curling, showing good flexibility (Fig. 4(e)). Consequently, the HEC-1150 °C sample was further characterized using TEM. Figure 4(f) displayed nanowires with smooth surfaces. High-resolution transmission electron microscopy (HRTEM) images further confirmed the single-crystal nature of HEC-1150 °C (Fig. 4(g)). The lattice fringe spacing of 0.26 nm corresponded to (111) plane spacing of the cubic high-entropy carbide phase (inset in Fig. 4(g)). Additionally, significant lattice distortions in the bulk phase resulted from different atomic dimensions of transition metals (Fig. 4(h)), leading to substantial conductive losses and dipole polarization losses. Figure 4(i) showed the catalyst alloy particle on the top of HEC nanowire. The EDS mapping and corresponding elemental distribution images of the

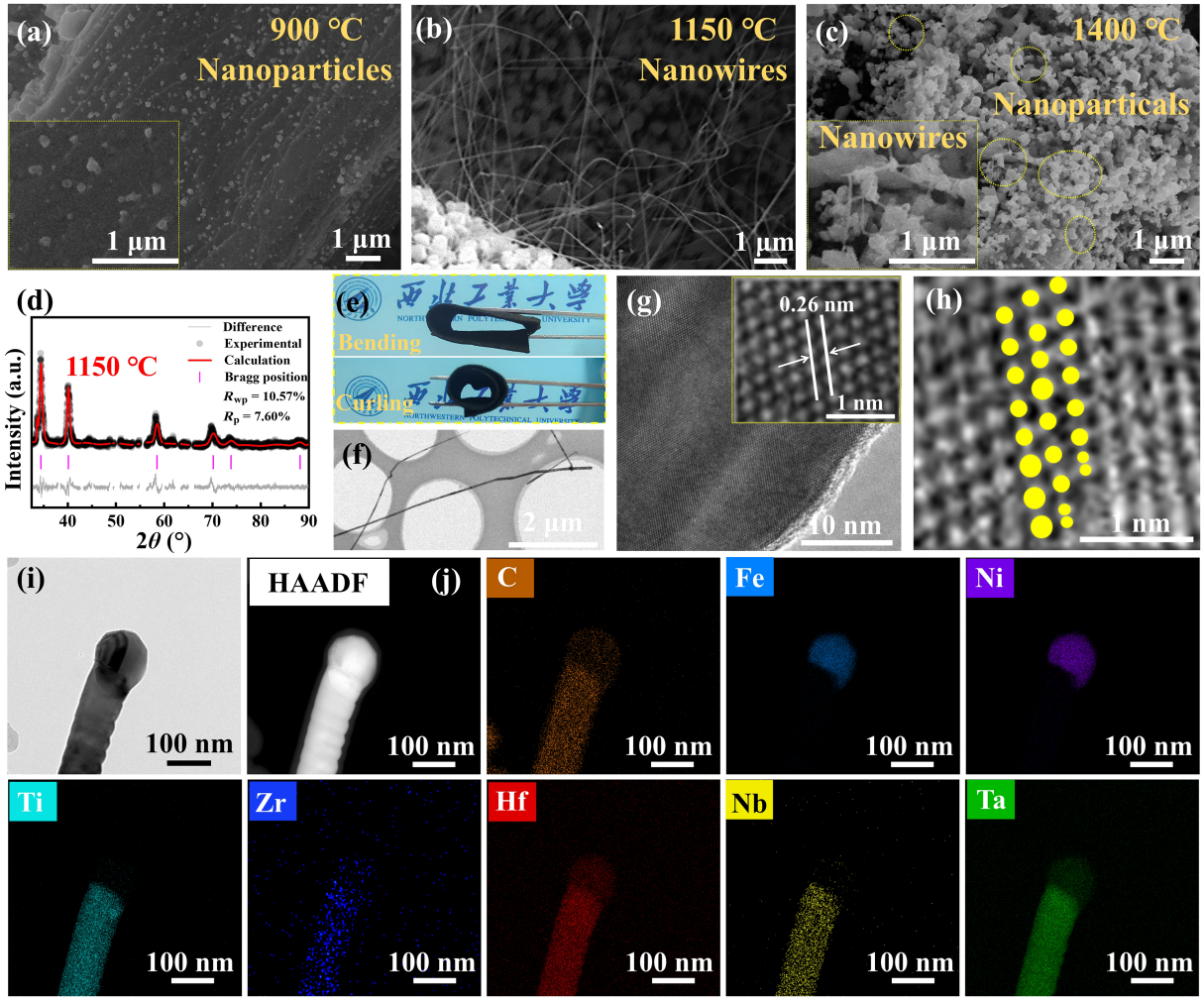

Figure 4 SEM images of (a) HEC-900 °C, (b) HEC-1150 °C, and (c) HEC-1400 °C. (d) Rietveld refinement of XRD data. (e) Digital photos of the flexibility of HEC-1150 °C. (f)TEM image of HEC nanowires. (g) HRTEM image (inset was the illustration of lattice fringe spacing), (h) illustration of lattice distortions, (i) TEM image, and (j) HAADF image and corresponding elemental mapping images of HEC nanowire.

catalyst alloy particles and nanowires in Fig. 4(j) revealed the distribution of C, Hf, Zr, Nb, Ta, Ti, Ni, and Fe. Fe and Ni elements accumulated at the tips of the nanowires, while C, Zr, Hf, Nb, Ti, and Ta were uniformly distributed HEC nanowires, further confirming the successful synthesis of HEC nanowires. The spherical catalyst particles were observed at the top of the nanowires, suggesting that the growth of the nanowires followed the VLS mechanism.

To understand the growth mechanism of the synthesis of HEC nanowires, Fig. 5 presented a schematic diagram. In this study, the reaction precursors for fabricating HEC nanowires primarily consisted of the metallic and carbon elements from the high-entropy precursor and the carbon from the cotton fabric. Compared to conventional carbon fiber cloth, the cotton fabric exhibited more uniform adsorption of raw materials (Fig. S3(a) in the ESM). Due to the smooth surface of the carbon fibers in carbon fiber cloth, loading capacity to the raw materials was also lower than that of cotton fabric (Fig. S3(b) in the ESM). Consequently, under identical thermal treatment conditions, no HEC nanowires were obtained on the carbon fiber substrate (Fig. S3(c) in the ESM). Thus, the cotton fabric not only served as a flexible substrate for HEC nanowire growth but also would provide enough reaction materials from itself and absorbed raw materials. Moreover, the spherical cap-shaped catalysts at the tops of the nanowires suggested that the generation of the HEC nanowires was guided by the classic VLS generation mechanism, which could be explained as follows [33]. Firstly, it should be noted that the system still contained oxygen due to the use of argon gas with a purity of 99.99% as the protective gas [34]. Additionally, there was oxygen adsorbed on the cotton fabric. Thus, in the initial stage, the transition metal elements from the high-entropy precursor reacted with the oxygen in the system to form transition metal oxides (TMO_x). Subsequently, TMO_x reacted with NaF to produce gaseous fluorides or oxyfluorides (TMO_xF_y) (Eq. (1)). At high temperature, the polymer precursor and cotton fabric generated carbon-based molecules, such as CO, CO_2, and CH_4. Then $Fe(NO_3)_2{\cdot}9H_2O$ and $Ni(NO_3)_2{\cdot}6H_2O$ reacted with these carbon-based molecules to form Fe-Ni alloy droplets (Eq. (2)). Thereafter, the produced gaseous TMO_xF_y reacted with carbon-based molecules to produce transition metals (TMs) (Eq. (3)). Carbon and the formed TMs dissolved into the molten alloy droplets via Eq. (4) [35, 36]. When the concentration of HEC molecules in the Fe-Ni alloy droplets attained a supersaturated state, HEC precipitated from the catalyst droplets to nucleate and grow. Additionally, HEC exhibited greater lattice distortion than conventional carbides, facilitating nanowire development [37].

$$TMO_x\,(s) + NaF\,(g, l) \rightarrow TMO_xF_y\,(g) + Na_2O\,(g) \quad (1)$$

$$Ni(NO_3)_2 \cdot 6H_2O\,(l) + Fe(NO_3)_2 \cdot 9H_2O\,(l) + 5C\,(s, g) \rightarrow Fe\text{-}Ni\,(l) + 5NO_2\,(g) + 5CO\,(g) + 15H_2O\,(g) \quad (2)$$

$$TMO_xF_y\,(g) + C\,(s, g) \rightarrow TMs\,(s, g) + CO_x\,(g) + y/2F_2\,(g) \quad (3)$$

$$TM + C \rightarrow (Ti_{0.2}Zr_{0.2}Hf_{0.2}Nb_{0.2}Ta_{0.2})C \quad (4)$$

In the initial stage, the vapor pressures of the carbon-based and gaseous TMO_xF_y products in the system were relatively high, resulting in the observation of high-entropy carbide particles on the CCF. As the reaction proceeded, the vapor pressures of the gaseous products in the system decreased to lower levels, which promoted the formation of HEC nanowires [38]. This explains the presence of ceramic particles on the CCF in the HEC-1150 °C.

There was a close relationship between electrical conductivity and EMI shielding capability [39]. Therefore, the electrical conductivity of the samples was measured. As shown in Fig. 6(a), the electrical conductivity of CCF was 150.15 S/m, indicating that it has a small contribution to EMI performance. The electrical conductivity of HEC-1150 °C was the highest (374.53 S/m), which was superior to that of HEC-900 °C (175.43 S/m) and HEC-1400 °C (155.76 S/m). This might be resulted from the formation of a more conductive network by HEC nanowires in HEC-1150 °C and the internal good electrical conductivity of HEC, providing more conductive pathways [40]. Generally, higher electrical conductivity enhances the conductive loss of electromagnetic waves, thereby improving EMI shielding performance.

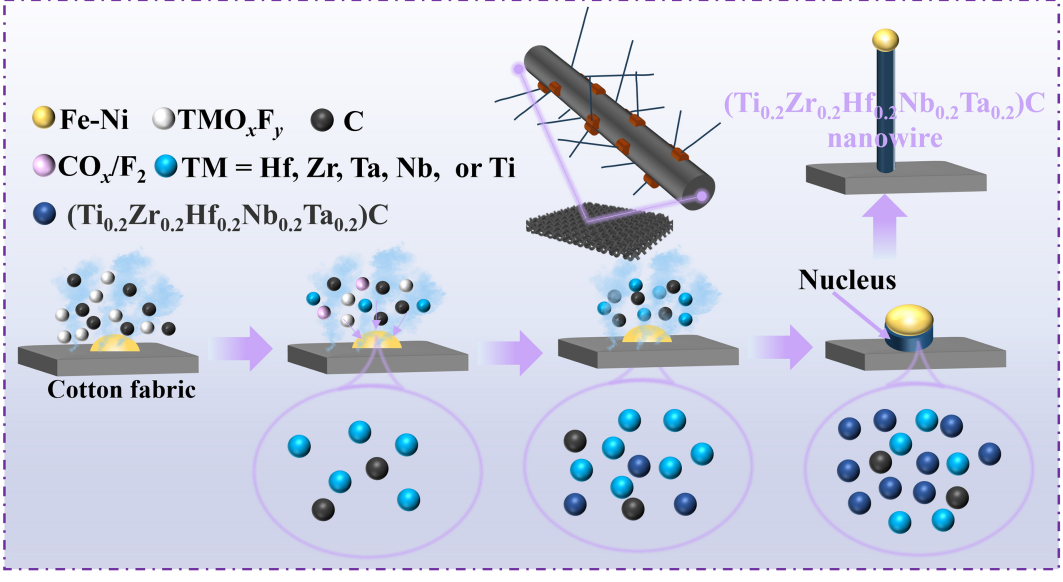

Figure 5 The possible growth mechanism of HEC nanowires.

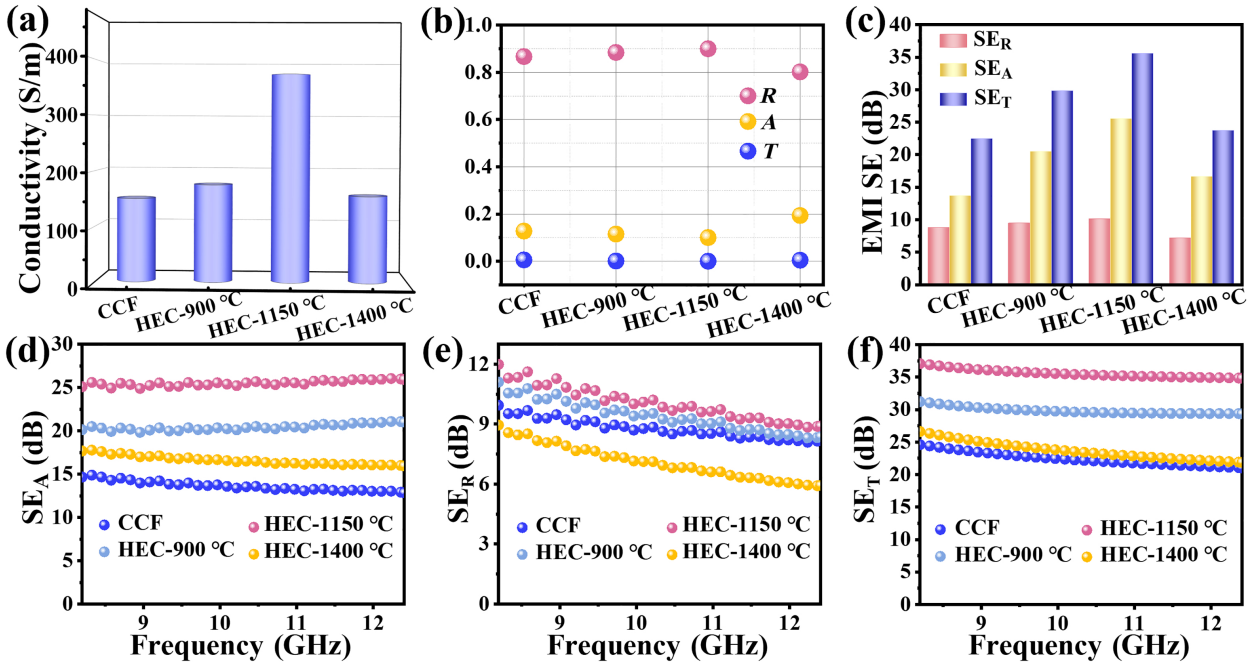

Figure 6 (a) Electrical conductivity; (b) average *R*, *T*, and *A*; (c) average SE_A, SE_T, and SE_R; (d) SE_A, (e) SE_R, and (f) SE_T of the samples in X-band.

To explore the EMI shielding mechanism, the *A*, *R*, and *T* parameters were obtained for specimens with nearly identical thicknesses of approximately 0.45 mm (Fig. 6(b)). All *R* values of the four samples were larger than their corresponding *A* values, indicating that their EMI shielding mechanisms was dominated by reflection. The HEC-1150 °C sample could reflect or absorb 99.9719854% of the electromagnetic waves. The EMI SE for the different samples was obtained, and the results were shown in Figs. 6(c)–6(f). The EMI shielding performance was ranked as follows: HEC-1150 °C > HEC-900 °C > HEC-1400 °C > CCF. Their average values in the X-band were 35.57, 29.83, 23.71, and 22.40 dB, respectively. These results correlated with the nanowire content and structural porosity. The lowest EMI SE of HEC-1400 °C might be because the fibers in the cotton fabric of HEC-1400 °C shrank and carbonized at high temperatures, resulting in larger pores (as shown in Fig. S4 in the ESM), which enabled more electromagnetic waves to transmit directly or undergo single-bounce reflection. The optimal EMI shielding performance of the HEC-1150 °C sample was attributed to the conductive network formed by CCF and HEC nanowires, and the polarization loss caused by the lattice distortion of high-entropy carbides.

Moreover, the EMI SE of HEC-1150 °C could be optimized over a wide range by adjusting its thickness. As shown in Fig. 7(a), the *R* values of HEC-1150 °C-1 (0.45 mm), HEC-1150 °C-2 (0.9 mm), and HEC-1150 °C-3 (1.35 mm) were all larger than their *A* values, which further confirmed that the dominant shielding mechanism of HEC-1150 °C was reflection [41]. The *T* value of HEC-1150 °C-3 was 3.31274×10^{-6}, indicating that it could shield over 99.999668726% of the electromagnetic waves. The EMI SE of the samples with different thicknesses was shown in Figs. 7(b) and 7(c). The EMI SE values of HEC-1150 °C-1, HEC-1150 °C-2, and HEC-1150 °C-3 were 35.57, 47.17, and 53.45 dB, respectively. The maximum EMI SE value of HEC-1150 °C-3 in the X-band was 57.55 dB (Figs. 7(b) and 7(c)). According to previous studies, electrical conductivity and thickness were key determinants of the SE_A. When thickness increased and conductivity improved, the skin depth decreased, thereby enhancing the capacity in preventing electromagnetic waves. Moreover, the markedly higher SE_A values compared with the SE_R values highlighted the importance of absorption in enhancing EMI shielding performance. When electromagnetic waves interacted with the surface of the materials, reflection occurred prior to absorption. Consequently, SE_A measured the capacity of the material to weaken waves that had entered its interior. Table S1 in the ESM compared the EMI performance of different shielding materials in the X-band. The HEC nanowires on cotton fabric in this work exhibit remarkable EMI shielding performance, achieving a relatively high EMI SE compared to recently published works [42–50].

A possible electromagnetic shielding mechanism of the HEC-1150 °C material was shown in Fig. 7(d). When electromagnetic waves were incident on the surface of HEC-1150 °C, most of them were reflected due to the impedance mismatch between air and the material. The dielectric dissipation in high-entropy carbides arose from the following factors: dipole polarization, conductive loss, and interface loss. [51]. When electromagnetic waves interacted with high-entropy carbides, heat was generated because of the flow of electric current, resulting in conductive loss. HEC constituted by different metal elements with different radii and electronegativities, led to dipole polarization and relaxation. Lattice distortion in HEC could lead to the formation of numerous metal vacancies. These vacancies could increase the density of states at the Fermi level, thereby enhancing the metallicity of HECs. Thus, the electrical conductivity was improved, resulting in conduction loss. Additionally, the defects caused by lattice distortion act as dipoles in the electromagnetic field. Through the frequent reorientation of these dipoles, the energy of electromagnetic waves could be largely dissipated, thereby increasing dipole polarization loss [52]. The crystal structure of HEC was complex and might contain various interfaces. The electromagnetic field caused an imbalance in the charge distribution on two sides of the interfaces, causing interface loss. Moreover, HECs were not ideal solid solutions, meaning that the atoms of different elements were not randomly distributed at

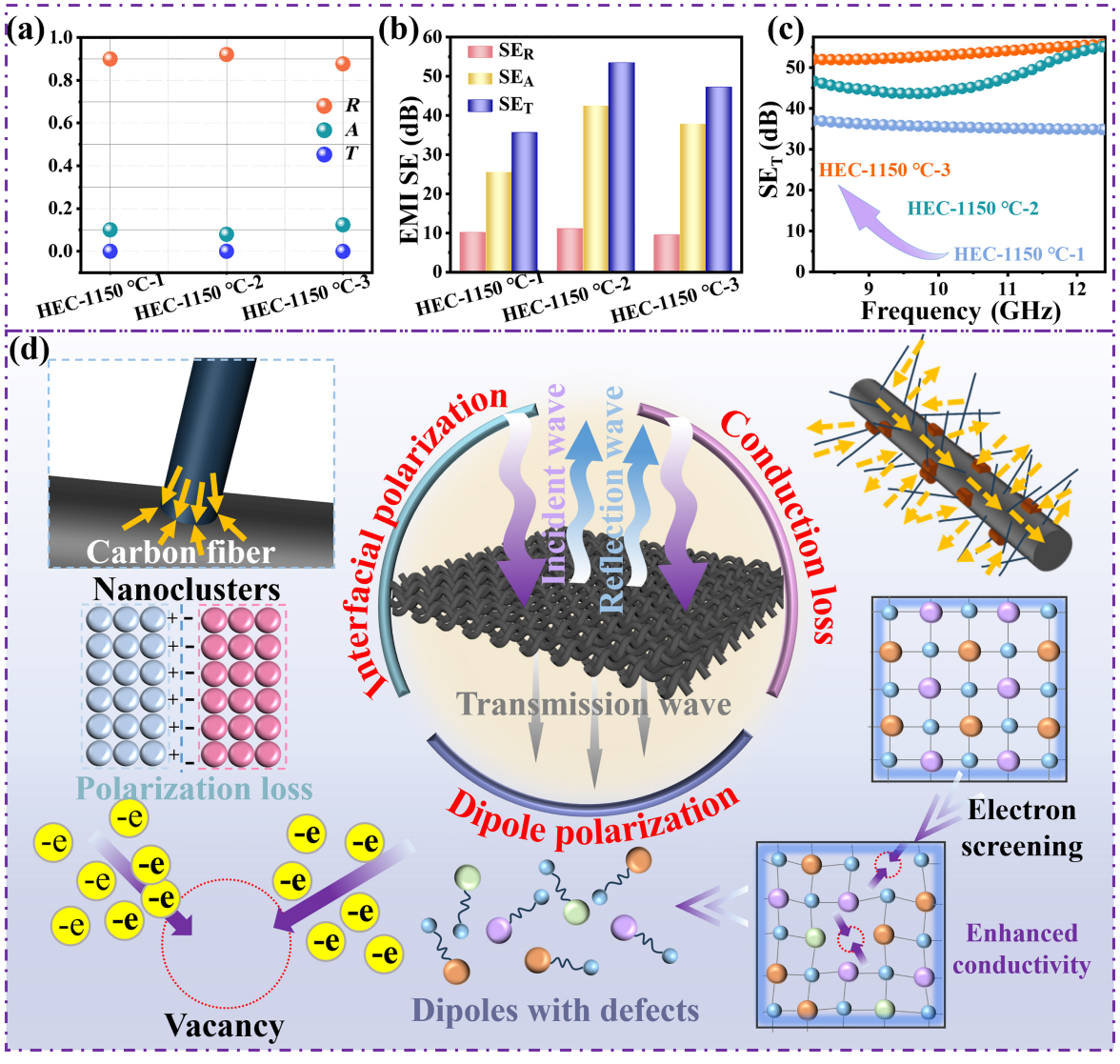

Figure 7 EMI shielding performance in X-band of HEC-1150 °C in diverse thicknesses. (a) Average *A*, *T*, and *R*; (b) average SE_R, SE_A, and SE_T; (c) SE_T; and (d) schematic representation of the EMI shielding mechanism for HEC-1150 °C.

the lattice sites. Instead, they exhibited local chemical order, leading to the formation of different nanoclusters. The interfaces of these nanoclusters impede electron transport, causing charge separation on either side of the interface, which enhanced interfacial losses [53]. Meanwhile, the heterostructure of CCF and nanowires also produced interface loss during the transmission of electromagnetic waves [54]. In addition, the conductive network of CCF, HEC nanowires, and particles was conducive to the attenuation of multiply reflected electromagnetic waves. All these factors contributed to the strong EMI shielding performance in HEC-1150 °C.

4 Conclusions

In this study, we successfully synthesized HEC nanowires on cotton fabric through polymer pyrolysis method. The cotton fabric served not only as a flexible substrate but also as a carbon source for the generation of nanowires. The growth mechanism of the HEC nanowires was Fe-Ni assisted VLS process. Furthermore, the EMI shielding performance of the HEC nanowires was evaluated, demonstrating an exceptional EMI SE of 57.55 dB with the thickness of 1.35 mm in 8.2–12.4 GHz. The exceptional EMI shielding performance was attributed to the conduction loss, additional dipole polarization loss and interfacial loss generated by HEC. This work introduces a scalable method for synthesizing high-quality HEC nanowires and also provides an in-depth insight into the growth procedure and EMI shielding properties and mechanism.

Electronic Supplementary Material: Supplementary material (MS profile of polymer precursor, C 1s spectra of HEC-1150 °C, comparison data of the loading of reaction raw materials between cotton fabric and carbon fiber cloth, EMI shielding performance comparisons, and etc.) is available in the online version of this article at https://doi.org/10.26599/NR.2025.94907749.

Data availability

All data needed to support the conclusions in the paper are presented in the manuscript and the Electronic Supplementary

Material. Additional data related to this paper may be requested from the corresponding author upon request.

Acknowledgements

This work was supported by the National Natural Science Foundation of China (Nos. 52202047, 524B2015, 52293370, and 52293371), China Postdoctoral Science Foundation (No. 2023T160530), and Joint Fund for Science and Technology Research of Henan Province and Henan Academy of Sciences (No. 235200810094).

Thanks eceshi (www.eceshi.com) for FT-IR, XPS and TG-DTG-MS test.

Declaration of competing interest

All the contributing authors report no conflict of interests in this work.

Author contribution statement

H. M. L.: Data curation, formal analysis, funding acquisition, writing – original draft. Y. J. S.: Investigation. X. Z.: Software. B. L.: validation. L. Y. H.: Resources, funding acquisition. Q. G. F.: Resources, supervision. X. M. Y.: Resources, project administration, funding acquisition, writing – review & editing. H. J. L.: Resources, supervision, project administration, funding acquisition.

Use of AI statement

None.

References

[1] Tian, X. F.; Li, H. J.; Shi, X. H.; Lin, H. J.; Yan, N. N.; Feng, T. Morphologies evolution and mechanical behaviors of SiC nanowires reinforced C/(PyC–SiC)$_n$ multilayered matrix composites. *J. Mater. Sci. Technol.* **2022**, *96*, 190–198.

[2] He, Q. C.; Li, H. J.; Yin, X. M.; Lu, J. H. Effects of PyC shell thickness on the microstructure, ablation resistance of SiCnws/PyC-C/C-ZrC-SiC composites. *J. Mater. Sci. Technol.* **2021**, *71*, 55–66.

[3] Yin, X. M.; Han, L. Y.; Liu, H. M.; Li, N.; Song, Q.; Fu, Q. G.; Zhang, Y. L.; Li, H. J. Recent progress in 1D nanostructures reinforced carbon/carbon composites. *Adv. Funct. Mater.* **2022**, *32*, 2204965.

[4] Yin, X. M.; Li, H. J.; Fu, Y. Q.; Yuan, R. M.; Lu, J. H. Hierarchical core–shell structure of $NiCo_2O_4$ nanosheets@HfC nanowires networks for high performance flexible solid-state hybrid supercapacitor. *Chem. Eng. J.* **2020**, *392*, 124820.

[5] Yin, X. M.; Li, H. J.; Han, L. Y.; Yuan, R. M.; Lu, J. H. $NiCo_2O_4$ nanosheets sheathed SiC@CNTs core–shell nanowires for high-performance flexible hybrid supercapacitors. *J. Colloid Interface Sci.* **2020**, *577*, 481–493.

[6] Liu, H. M.; Li, K. Z.; Zhang, X.; Yin, X. M.; Fu, Q. G.; Li, H. J. SiC nanomaterials and their derived carbons for high-performance supercapacitors. *Acta Phys.-Chim. Sin.* **2023**, *40*, 2304026.

[7] Yu, R. W.; Liu, Y. W.; Sun, X. H.; He, G.; Dong, H.; Deng, S. X.; Li, J. T.; Chu, Y. H. Composition engineering of high-entropy diboride nanoparticles for efficient catalytic degradation of antibiotics. *Sci. China Mater.* **2023**, *66*, 3582–3591.

[8] Wen, T. Q.; Ye, B. L.; Nguyen, M. C.; Ma, M. D.; Chu, Y. H. Thermophysical and mechanical properties of novel high-entropy metal nitride-carbides. *J. Am. Ceram. Soc.* **2020**, *103*, 6475–6489.

[9] Jiang, B. B.; Yu, Y.; Cui, J.; Liu, X. X.; Xie, L.; Liao, J. C.; Zhang, Q. H.; Huang, Y.; Ning, S. C.; Jia, B. H. et al. High-entropy-stabilized chalcogenides with high thermoelectric performance. *Science* **2021**, *371*, 830–834.

[10] Wang, H. Y.; Shi, Y.; Li, M.; Ye, Y. X.; Zhang, Y. Z.; Rong, T.; Wang, Z. M.; Zhang, J. K.; Chen, H.; Tao, Y. et al. High-entropy 1T-phase quantum sheets of transition-metal disulfides. *Adv. Mater.* **2025**, *37*, 202500321.

[11] Na, F.; Li, X.; Wang, J.; Cheng, X. M.; Zhang, J.; Wang, Y. L.; Lin, H. Z.; Zhan, L.; Ling, L. C.; Zhang, Y. Z. Immobilizing single atom on high-entropy oxides as separator regulators for catalyzing low-temperature lithium-sulfur battery. *Energy Stor. Mater.* **2025**, *78*, 104228.

[12] Sun, Q. C.; Tan, H.; Zhu, S. Y.; Zhu, Z. X.; Wang, L.; Cheng, J.; Yang, J. Single-phase (Hf-Mo-Nb-Ta-Ti)C high-entropy ceramic: A potential high temperature anti-wear material. *Tribol. Int.* **2021**, *157*, 106883.

[13] Zhu, Z. J.; Liu, Y. W.; Qin, Y. B.; Gu, F. C.; Zhuang, L.; Yu, H. L.; Chu, Y. H. Tough and strong bioinspired high-entropy all-ceramics with a contiguous network structure. *Nat. Commun.* **2025**, *16*, 4587.

[14] Ma, M. D.; Hu, X. F.; Meng, H.; Zhao, Z. S.; Chang, K. K.; Chu, Y. H. High-entropy metal carbide nanowires. *Cell Rep. Phys. Sci.* **2022**, *3*, 100839.

[15] Zhu, Y. J.; Guan, L.; Duan, C. Q.; Zhang, J. X.; Yan, Z. K.; Wen, L. C.; Wang, Z. H.; Sun, X. X.; Yao, Y. L.; Guo, X. Q. et al. High-entropy transition metal carbide nanowires with enhanced microwave absorption properties. *J. Mater. Sci. Technol.* **2025**, *224*, 302–311.

[16] Du, Z. G.; Wu, C.; Chen, Y. C.; Cao, Z. J.; Hu, R. M.; Zhang, Y. Z.; Gu, J. N.; Cui, Y. L. S.; Chen, H.; Shi, Y. Z. et al. High-entropy atomic layers of transition-metal carbides (MXenes). *Adv. Mater.* **2021**, *33*, 2101473.

[17] Zhuang, L.; Wen, Z. H.; Liu, Y. W.; Yang, J.; Yu, H. L.; Chu, Y. H. Unveiling the oxidation mechanisms of high-entropy carbides through atomic-scale dynamic observation. *Adv. Mater.* **2025**, *37*, 202417846.

[18] Zhao, J. H.; Zhang, Y. L.; Chen, H.; Fu, Y. Q.; Miao, Q.; Meng, J. C.; Li, J. C. Single-source precursor derived high-entropy metal-carbide nanowires: Microstructure and growth evolution. *J. Adv. Ceram.* **2023**, *12*, 2041–2052.

[19] Liu, H. M.; Zhang, X.; Li, K. Z.; Cui, Q. A.; Shen, Q. L.; Li, H. J.; Yin, X. M. Functional integrated electromagnetic interference shielding in supercapacitors based on aligned SiC nanowires decorated vertical graphene nanosheets. *Carbon* **2024**, *220*, 118864.

[20] Liu, H. M.; Zhang, X.; Li, K. Z.; Cui, Q. A.; Han, L. Y.; Shen, Q. L.; Li, H. J.; Yin, X. M. Construction of core–shell structured SiC nanowires@carbon nanotubes hybrid conductive network for supercapacitors and electromagnetic interference shielding. *Carbon* **2024**, *228*, 119411.

[21] Liu, H. H.; Du, B.; Chu, Y. H. Synthesis of the ternary metal carbide solid-solution ceramics by polymer-derived-ceramic route. *J. Am. Ceram. Soc.* **2020**, *103*, 2970–2974.

[22] Du, B.; Liu, H. H.; Chu, Y. H. Fabrication and characterization of polymer-derived high-entropy carbide ceramic powders. *J. Am. Ceram. Soc.* **2020**, *103*, 4063–4068.

[23] Cai, F. Y.; Ni, D. W.; Chen, B. W.; Ye, L.; Sun, Y. N.; Lu, J.; Zou, X. G.; Zhou, H. J.; He, P.; Zhao, T. et al. Fabrication and properties of Cf/$(Ti_{0.2}Zr_{0.2}Hf_{0.2}Nb_{0.2}Ta_{0.2})$C–SiC high-entropy ceramic matrix composites via precursor infiltration and pyrolysis. *J. Eur. Ceram. Soc.* **2021**, *41*, 5863–5871.

[24] Lu, Y.; Sun, Y. N.; Zhang, T. Z.; Chen, F. H.; Ye, L.; Zhao, T. Polymer-derived Ta_4HfC_5 nanoscale ultrahigh-temperature ceramics: Synthesis, microstructure and properties. *J. Eur. Ceram. Soc.* **2019**, *39*, 205–211.

[25] Wang, Y. C.; Csanádi, T.; Zhang, H. F.; Dusza, J.; Reece, M. J. Synthesis, microstructure, and mechanical properties of novel high entropy carbonitrides. *Acta Mater.* **2022**, *231*, 117887.

[26] Wang, Y. M.; Zhang, C. H. Reduced graphene oxide derived from low-grade coal for high-performance flexible supercapacitors with

ultrahigh cyclability. *Nanomaterials* **2022**, *12*, 2989.
[27] Fang, D.; Wang, C.; Lv, C. H.; Lv, Y. M.; Huang, G. L.; Yang, J. Y.; Pan, S. X. XPS studies of surface oxidation of metal carbides. *Fullerenes Nanotubes Carbon Nanostruct.* **2022**, *30*, 718–726.
[28] Hauser, D.; Auer, A.; Kunze-Liebhäuser, J.; Schwarz, S.; Bernardi, J.; Penner, S. Hybrid synthesis of zirconium oxycarbide nanopowders with defined and controlled composition. *RSC Adv.* **2019**, *9*, 3151–3156.
[29] Vargas, M.; Castillo, H. A.; Restrepo-Parra, E.; De La Cruz, W. Stoichiometry behavior of TaN, TaCN and TaC thin films produced by magnetron sputtering. *Appl. Surf. Sci.* **2013**, *279*, 7–12.
[30] Jalaly, M.; Gotor, F. J.; Sayagués, M. J. Mechanochemical combustion synthesis of vanadium carbide (VC), niobium carbide (NbC) and tantalum carbide (TaC) nanoparticles. *Int. J. Refract. Met. Hard Mater.* **2019**, *79*, 177–184.
[31] Oghenevweta, J. E.; Wexler, D.; Calka, A. Study of reaction sequences during MSR synthesis of TiC by controlled ball milling of titanium and graphite. *Mater. Charact.* **2018**, *140*, 299–311.
[32] Niu, B.; Cai, D. L.; Yang, Z. H.; Duan, X. M.; Duan, W. J.; Qiu, B. F.; Li, Q.; He, P. G.; Jia, D. C.; Zhou, Y. Effects of sintering temperature on the microstructure and properties of h-BN ceramics with MAS as liquid sintering aid. *Ceram. Int.* **2020**, *46*, 1076–1082.
[33] Tao, X. Y.; Li, Y. P.; Du, J.; Xia, Y.; Yang, Y. C.; Huang, H.; Gan, Y. P.; Zhang, W. K.; Li, X. D. A generic bamboo-based carbothermal method for preparing carbide (SiC, B_4C, TiC, TaC, NbC, $Ti_xNb_{1-x}C$, and $Ta_xNb_{1-x}C$) nanowires. *J Mater Chem.* **2011**, *21*, 9095–9102.
[34] Wu, R. B.; Li, B. S.; Gao, M. X.; Chen, J. J.; Zhu, Q. M.; Pan, Y. Tuning the morphologies of SiC nanowires via the control of growth temperature, and their photoluminescence properties. *Nanotechnology* **2008**, *19*, 335602.
[35] Ning, S. S.; Wen, T. Q.; Ye, B. L.; Chu, Y. H. Low-temperature molten salt synthesis of high-entropy carbide nanopowders. *J. Am. Ceram. Soc.* **2020**, *103*, 2244–2251.
[36] Liu, D.; Liu, H. H.; Ning, S. S.; Chu, Y. H. Chrysanthemum-like high-entropy diboride nanoflowers: A new class of high-entropy nanomaterials. *J. Adv. Ceram.* **2020**, *9*, 339–348.
[37] Song, N. N.; Li, X. D. Unveiling polytype transformation assisted growth mechanism in boron carbide nanowires. *J. Cryst. Growth* **2018**, *481*, 11–17.
[38] Chu, Y. H.; Jing, S. Y.; Chen, J. K. *In situ* synthesis of homogeneously dispersed SiC nanowires in reaction sintered silicon-based ceramic powders. *Ceram. Int.* **2018**, *44*, 6681–6685.
[39] Han, L. Y.; Li, K. Z.; Liu, H. M.; Jiao, Y. M.; Yin, X. M.; Li, H. J.; Song, Q.; Qi, L. H. Heterogeneous stacking strategy towards carbon aerogel for thermal management and electromagnetic interference shielding. *Chem. Eng. J.* **2023**, *465*, 142839.
[40] Zhou, Y. C.; Zhao, B.; Chen, H.; Xiang, H. M.; Dai, F. Z.; Wu, S. J.; Xu, W. Electromagnetic wave absorbing properties of TMCs (TM = Ti, Zr, Hf, Nb and Ta) and high entropy $(Ti_{0.2}Zr_{0.2}Hf_{0.2}Nb_{0.2}Ta_{0.2})C$. *J. Mater. Sci. Technol.* **2021**, *74*, 105–118.
[41] Han, L. Y.; Li, K. Z.; Fu, Y. Q.; Yin, X. M.; Jiao, Y. M.; Song, Q. Multifunctional electromagnetic interference shielding 3D reduced graphene oxide/vertical edge-rich graphene/epoxy nanocomposites with remarkable thermal management performance. *Compos. Sci. Technol.* **2022**, *222*, 109407.
[42] Choi, Y. W.; Hwang, U.; Ho, J. W.; Park, W.; Hassan, T.; Koo, C. M.; Nam, J. D.; Song, Y. J.; Yoo, P. J. Enhanced electromagnetic interference shielding in cement composites utilizing carbon fiber clustered networks with dual different lengths. *Carbon* **2025**, *233*, 119887.
[43] Ren, Q.; Wei, Y. Q.; Li, X. Y.; Yu, C.; Wang, L.; Shen, B.; Zheng, W. G. Influence of expansion ratio and multilayered gradient structure on the electromagnetic interference shielding performance of lightweight poly (lactic acid)/carbon nanostructures composite foams. *Compos. Sci. Technol.* **2025**, *261*, 110992.
[44] Zhang, W. R.; He, Z. J.; Xie, J. L.; Su, F. F.; Xin, Y. Y.; Yao, D. D.; Li, M. X.; Wang, Y. D.; Zheng, Y. P. Flexible multifunctional polydimethylsiloxane composites with segregated structure fabricated by hydrophobic interaction for efficient electromagnetic interference shielding. *J. Mater. Sci. Technol.* **2025**, *220*, 67–77.
[45] Ouyang, W. C.; Mei, L.; Liu, Q.; Ding, C. B.; Liu, Y. M.; Zhao, C. W.; Xu, L. M.; Lu, F.; Luo, D. P.; Miao, C. G. et al. Ultrathin-flexible multifunctional MXene composite hydrogels with good mechanical properties-high strain sensitivity and ultra-broadband EMI shielding performances. *Chem. Eng. J.* **2024**, *494*, 153068.
[46] Jiang, D. X.; Tian, S.; Li, H. J.; Du, Z. W.; Liu, T.; Yan, D. K.; Zhou, L.; Bai, S.; Qiang, X. F. Lightweight HfC nanowire-carbon fiber/graphene aerogel composites for high-efficiency electromagnetic interference shielding. *Carbon* **2024**, *219*, 118788.
[47] Yang, Y. H.; You, X.; Ouyang, H. Y.; Xing, Z. Z.; Ren, M. H.; Zhang, Q. Q.; Zhang, X. Y.; Yang, J. S.; Dong, S. M. Electromagnetic interference shielding properties of foamed SiCnws/SiC composites reinforced by *in-situ* grown carbon nanofibers. *J. Alloy. Compd.* **2024**, *1008*, 176641.
[48] Chen, C. Z.; Feng, W. Y.; Wu, W. X.; Yu, Y. Y.; Qian, G. F.; Fu, L. H.; Min, D. Y. A highly strong PEDOT modified wood towards efficient electromagnetic interference shielding. *Ind. Crops Prod.* **2023**, *202*, 117109.
[49] Luo, J. M.; Yang, X. Q.; Xue, Y.; Yang, C. X.; Yang, Z. H.; Cai, Z. X.; Liu, Y.; Ma, Y.; Zhang, H.; Yu, J. Y. High-performance, multifunctional, and designable carbon fiber felt skeleton epoxy resin composites EP/CF-$(CNT/AgBNs)_x$ for thermal conductivity and electromagnetic interference shielding. *Small* **2024**, *20*, 2306828.
[50] Hu, Y.; Yang, G. Y.; Chen, J. Z.; Li, Y. J.; Dong, M.; Zhang, H.; Bilotti, E.; Jiang, J. J.; Papageorgiou, D. G. Interfacial engineering of hybrid MXene-Ni-CF tri-core–shell composites for electromagnetic interference shielding and E-heating applications. *Composites Part A: Appl. Sci. Manuf.* **2024**, *178*, 107990.
[51] Zhang, J. T.; Wang, W. L.; Zhang, Z. X.; Chen, J. Q.; Sun, X. N.; Sun, G. X.; Liang, Y. J.; Han, G. F.; Zhang, W. B. Synthesis, microstructure and electromagnetic wave absorption properties of high-entropy carbide powders. *J. Alloy. Compd.* **2023**, *966*, 171593.
[52] Hu, Y.; Ni, D. W.; Chen, B. W.; Cai, F. Y.; Liao, C. J.; Ding, Y. S.; Dong, S. M. C_f@BN/(CrZrHfNbTa)C–SiC high-entropy ceramic matrix composites with outstanding electromagnetic interference shielding and high-temperature resistance. *Ceram. Int.* **2024**, *50*, 38582–38591.
[53] Gu, F. C.; Wang, W.; Meng, H.; Liu, Y. W.; Zhuang, L.; Yu, H. L.; Chu, Y. H. Lattice distortion boosted exceptional electromagnetic wave absorption in high-entropy diborides. *Matter* **2025**, *8*, 102004.
[54] He, X.; Feng, L.; Zhang, Z.; Hou, X. J.; Ye, X. H.; Song, Q.; Yang, Y. L.; Suo, G. Q.; Zhang, L.; Fu, Q. G. et al. High-performance multifunctional carbon-silicon carbide composites with strengthened reduced graphene oxide. *ACS Nano* **2021**, *15*, 2880–2892.